HHS Public Access

Author manuscript

Nat Biomed Eng. Author manuscript; available in PMC 2021 March 28.

Published in final edited form as:

Nat Biomed Eng. 2021 March ; 5(3): 264–277. doi:10.1038/s41551-020-00616-6.

AND-gate contrast agents for enhanced fluorescence-guided surgery

John C. Widen[1], **Martina Tholen**[1], **Joshua J. Yim**[1,2], **Alexander Antaris**[7], **Kerriann M. Casey**[4], **Stephan Rogalla**[5,6], **Alwin Klaassen**[7], **Jonathan Sorger**[7], **Matthew Bogyo**[1,2,3,*]

[1]Department of Pathology, Stanford University School of Medicine, 300 Pasteur Drive, Stanford, California, USA

[2]Department of Chemical and Systems Biology, Stanford University School of Medicine, 300 Pasteur Drive, Stanford, California, USA

[3]Department of Microbiology and Immunology, Stanford University School of Medicine, 300 Pasteur Drive, Stanford, California, USA

[4]Department of Comparative Medicine, Stanford University School of Medicine, 300 Pasteur Drive, Stanford, California, USA

[5]Department of Medicine, Division of Gastroenterology and Hepatology, Stanford University School of Medicine, 300 Pasteur Drive, Stanford, California, USA

[6]Department of Radiology, Stanford University School of Medicine, 300 Pasteur Drive, Stanford, California, USA

[7]Intuitive Surgical Inc., 1020 Kifer Road, Sunnyvale, California 94086, United States

Abstract

The surgical resection of tumours requires the precise location and definition of the margins between lesions and normal tissue. However, this is made difficult by irregular margin borders. Although molecularly targeted optical contrast agents can be used to define tumour margins during surgery in real time, the selectivity of the contrast agents is often limited by the target being expressed in both healthy and tumour tissues. Here, we show that AND-gate optical imaging probes requiring the processing of two substrates by multiple tumour-specific enzymes produce a

[*]**Correspondence and requests for materials** should be addressed to mbogyo@stanford.edu.

Author contributions

M.B. and J.C.W conceived of the AND-Gate probe concept and designed all experiments. J.C.W synthesized all AND-Gate probes, conducted the fluorogenic substrate assays, live and fixed cell fluorescent microscopy experiments, and mouse model experiments. J.C.W and M.B. wrote the text of the paper and constructed the figures with input from J.J.Y. and K.C.M. M.T. and J.J.Y helped perform live and *ex vivo* imaging during the 4T1 cancer mouse model experiment including dissection of the mice. M.T. aided in the immunohistochemical analysis of 4T1 tumors. A.A, A.K., and J.S. assisted with the robotic surgery. K.M.C. evaluated H&E sections for the colorectal and 4T1 breast cancer mouse models.

Supplementary information is available for this paper at https://doi.org/10.1038/s41551-01X-XXXX-X.

fluorescent signal with significantly improved specificity and sensitivity to tumour tissue. We evaluated the performance of the probes in mouse models of mammary tumours and of metastatic lung cancer, and during fluorescence-guided robotic surgery. Imaging probes relying on multivariate activation to selectively target complex patterns of enzymatic activity should be useful in disease detection, treatment and monitoring.

For many cancers, surgery is the primary treatment option followed by chemo and/or radiation therapy. Early detection and surgical removal of solid tumors currently remain the most effective way to produce a curative result. Success outcomes are highly dependent on how effectively the tumor tissue can be identified[1,2]. Accurate detection of the 'margin' between tumor and normal healthy tissues is essential to prevent either incomplete removal of tumor cells leading to increased recurrence rates (up to 30–65% of cases)[3–5] or removal of excess healthy tissue. Furthermore, solid tumors derived from different tissues and cell types can have dramatically different margin borders, making the prospects for complete removal highly variable[6]. In fact, rates of repeat surgeries for some cancer types (i.e. breast) are between 20 and 50%[2,7]. Therefore, methods that allow both selective and sensitive real-time detection of tumor margins have the potential to significantly impact surgical treatment outcomes of many of the most common types of cancer. For most surgical treatments for cancer, imaging methods such as Magnetic Resonance Imaging (MRI), Positron Emission Tomography (PET), Single-Photon Emission Computerized Tomography (SPECT) and Computerized Tomography (CT) are used to diagnose and then identify the location of tumors[8]. However, these methods are not easily used intra-operatively due to the need for large instrumentation and/or ionizing radiation. They also typically do not provide sufficient sensitivity and resolution to allow identification of microscopic processes at the tumor margin. Alternatively, various analytical methods can be used to detect specific molecular signatures in real-time during a surgical procedure. This includes the use of mass spectrometry (MS), radio frequency (RF), ultrasound and fluorescence lifetime detectors that allow measurement of specific analytical signatures in the tumor microenvironment that set it apart from the surrounding normal tissues[9–11]. However, while these types of real-time analytical devices can be highly sensitive and accurate, they all are limited by issues related to sampling error and slow processing times since they require scanning of regions suspected to contain residual cancer.

As an alternative to the use of analytical detectors to scan tissues, systemically delivered optical contrast agents have the potential to broadly highlight tumor sites without any prior knowledge of tumor location[1,12]. Currently, there are only a few optical agents that are approved by the Food and Drug Administration (FDA) for use in humans and that are suitable for use with clinical camera systems. While there has been significant clinical benefit from dyes such as indocyanine green (ICG)[13] and 5-aminolevulinic acid (5-ALA)[14], the main limitation is their overall non-specific mechanism of action resulting in insufficient sensitivity and selectivity for use in diverse cancer types. A number of pre-clinical and early-stage clinical trials have begun for fluorescently tagged affinity agents such as antibodies, peptides and small molecule ligands[1,12,15]. There have also been significant advances in the development of "smart" probes that only produce a fluorescent signal when processed by a tumor-specific enzyme (Fig. 1a). This leads to a further increase in contrast because free

probe outside the tumor remains unprocessed and is not fluorescent. Proteases have become the enzymes of choice for generation of smart probes because short peptide substrates can be decorated with suitable fluorophore/quencher pairs such that probes are optically silent until cleaved by a protease[16–19]. Protease activity can also be used to process probes that then change their localization to be retained in cells within the tumor microenvironment[18,20]. Multiple proteases have proven to be useful biomarkers of cancerous tissues[21–24].

Previously, we designed a cysteine cathepsin-cleavable Near-Infrared (NIR) substrate probe 6QC-NIR[20]. Cleavage of this substrate probe produces high signals in cancers of the lung, breast, and colon, which can be detected with the FDA-approved da Vinci® Si Surgical System equipped with the Firefly® detection system[20]. We have found that further optimization of the reporter dye on this probe can greatly enhance its use with clinical camera systems[25]. However, the single biggest limitation to the use of protease substrates is their lack of selectivity that results from activity of a protease or protease family in healthy tissues as well as inside the tumor microenvironment. Here we describe a way to increase the overall tumor-selectivity by designing multivariate ‘AND-Gate’ probes in which multiple reporters must be processed within the tumor microenvironment to produce a specific optical signal (Fig. 1b–c). The term AND-Gate is a Boolean logic gate most commonly used in computer science, but also represents the behavior of molecular systems that require two orthogonal inputs to produce a single output[26]. Thus, selectivity can be greatly enhanced because identification of the tumor tissue is made using multiple markers that help to distinguish it from the surrounding normal tissues. In the current study, we demonstrate the utility of the approach using probes that contain substrates for the lysosomal cysteine cathepsins found in tumor associated macrophages, executioner caspases that are activated only in apoptotic cells, and fibroblast activation protein α (FAP) found at invasive edges of tumors. The resulting AND-Gate probes have greatly improved tumor selectivity due to the relatively high levels of apoptosis in tumors compared to surrounding normal healthy tissues and elevated activity of FAP in the tumor microenvironment. In addition, we find that AND-Gate probes have enhanced fluorescent signal within tumors compared to the corresponding cathepsin-only probe. These improved properties of the AND-Gate probes suggest that this will be a general strategy that can be used with diverse enzyme substrates to increase the selectivity of optical contrast agents.

Results

Design, testing and optimization of AND-Gate Probes

The design of a general ‘AND-Gate’ strategy involves placement of a fluorescent reporter in a central location such that multiple quenchers can be attached through linkages that are severed by the action of enzymes. This type of ‘hub and spoke’ model requires removal of all quenchers along the spokes to liberate the central fluorescent hub. In theory, the quencher groups can be attached to the central hub using any type of enzyme-sensitive linkage resulting in AND-Gates that are responsive to a diverse array of enzyme signatures. We choose to test this design strategy using a simple glutamic acid (Glu) central linker containing a fluorescent dye linked to quenchers through distinct peptide sequences that could be orthogonally cleaved by two proteases with non-overlapping substrate specificities.

The central Glu linker is ideal because a sulfo-Cy5 fluorophore can be attached to its free α-amine and each peptide substrate containing a sulfo-QSY21 quencher can be connected through amide bonds to the remaining carboxylic acids (Fig. 2a). This positions the quenchers such that fluorescence activation occurs only after both peptides have been cleaved. Furthermore, by using diamino-alkyl linkers between the peptides and the Glu core, the final fluorescent fragment will contain two free amine groups that induce lysosomal accumulation of the probe, as we have demonstrated for our cathepsin substrate probes[20].

We chose peptide substrates that have already been shown to be specifically processed by caspase 3 (Casp3; DEVDGP)[27] and the cysteine cathepsins (Cats; z-FK)[28]. These sequences are optimal for a first generation AND-Gate probe because Casp3 and Cats have highly orthogonal substrate specificities and therefore each protease can only process its corresponding substrate. Although these substrate sequences are selective for the protease or class of proteases, non-specific activation still occurs *in vivo* for all single substrate probes to some extent. The AND-Gate strategy diminishes this non-specific activation by requiring both processing events to be present in the same location. A subset of Cats are upregulated in both tumor associated macrophages (TAMs)[29–31] and present in most normal tissues, while Casp3 activity is elevated in tumors but is generally not active in healthy cells, except during development[32]. Because Casp3 activity occurs in the cytosol of apoptotic cells with compromised cell membranes, probes targeting this protease require a mechanism to induce accumulation[33,34]. We expected processing by Cats coupled with Casp3 would induce lysosomal accumulation of the processed AND-Gate probe. Additionally, both proteases are active within tumors but not expected to be active together in healthy tissues, making them ideal targets for our AND-Gate probe strategy.

We synthesized a first-generation AND-Gate probe, **DEATH-CAT 1,** containing the natural (L)-Glu central linker (Fig. 2a, Supplementary Scheme 1). We also synthesized negative controls in which a (D)-Asp (D-aspartic acid) was used in place of the natural (L)-Asp in the P1 position of the Casp3 sequence (**(D)-Asp 1**) and a (D)-Phe (D-phenylalanine) was used in the P2 position of the Cat sequence (**(D)-Phe 1**). To test the **DEATH-CAT 1** probe, we incubated it with recombinant human CatL, B, S, or Casp3 either separately or sequentially in combinations (Supplementary Fig. 1a, b). Importantly, we found that the probe only produced a fluorescent signal when both cathepsin and Casp3 were incubated sequentially. We also found that both control probes remained non-fluorescent after incubation with both proteases, regardless of order of addition, thus validating the overall concept of the AND-Gate strategy (Supplementary Fig. 1c, d). We then tested the stability of the linker using total tissue lysates derived from homogenized 4T1 breast tumors (Supplementary Fig. 1e). We found that, as expected, the **DEATH-CAT 1** probe was activated and the **(D)-Asp 1** negative control remained non-fluorescent. However, the **(D)-Phe 1** probe was activated in 4T1 lysate. Because the **(D)-Phe 1** probe was not cleaved by the purified cathepsins, the results from the lysate suggest that it is likely cleaved by hydrolysis of the glutamine amide in the linker by other enzymes to release the Cat sequence (z-FK) and produce the observed fluorescent signal.

Given the instability at the glutamine α-acid, we synthesized a 2nd generation probe **DEATH-CAT 2** and the respective negative controls **(D)-Phe 2** and **(D)-Asp 2**, in which the

natural (L)-Glu was replaced by the unnatural (D)-Glu (Fig. 2a, Supplementary Scheme 2). We evaluated this 2nd generation set of probes using the *in vitro* fluorogenic assay with recombinant proteases and found that the probes performed similarly to the first generation probes with only **DEATH-CAT 2** producing signal, and only after addition of both CatL and Casp3 (Fig. 2b,c). Using LC-MS analysis, we were able to detect the expected cleavage products after incubation with CatL or Casp3 alone, and with both proteases successively (Supplementary Fig. 2). Importantly, the second-generation negative control probes containing the (D)-Glu linker showed good stability in tumor lysates, with both remaining inactive even after 2 hours of incubation (Fig. 2d). Interestingly, **DEATH-CAT 2** was activated at a faster rate and with an overall higher signal than **6QC** in tumor lysate. The **DEATH-CAT 2** was also selective for Casp3 over other related initiator and executioner caspases (Supplementary Fig. 3).

Having solved the issue of linker stability, we tested the specificity of activation of the **DEATH-CAT 2** probe using a co-culture of breast tumor 4T1 cells and RAW macrophages. Cells were first incubated with dimethyl sulfoxide (DMSO) or the cytotoxic agent etoposide (5 μM) for 24 h to induce apoptosis. The **6QC**, **DEATH-CAT 2**, **Casp3-QC** (single substrate probe for Casp3, Supplementary Fig. 4), and respective negative control probes were added to the cells for 2 h before acquiring images (Fig. 2e, Supplementary Fig. 5). Sufficient fluorescence activation of **DEATH-CAT 2** compared to background was achieved within 2 h. At later time points, a large portion of cells have died, which reduces the number of adherent cells for imaging. As expected, none of the negative control probes were activated under either condition while **6QC** was activated independently of apoptosis induction and **DEATH-CAT 2** was activated only in the apoptotic cells (Fig. 2e, f). These results confirm that the **DEATH-CAT 2** probe required processing by both proteases to produce a fluorescent product that accumulates inside macrophage lysosomes.

AND-Gate Probes improve tumor selectivity *in vivo*

We next evaluated the **DEATH-CAT 2** probe and its respective negative controls in a 4T1 mouse model of breast cancer. We chose this model because it allows direct imaging of live animals using a NIR imaging system. The tumor-specific signal can be measured relative to surrounding background tissues and tissues can be subsequently removed for quantification and determination of overall probe activation in major organs distant to the tumor site. We imaged live animals 2 h post injection of probes and found that the **DEATH-CAT 2** probe showed strong tumor accumulation that resulted in a brighter tumor signal than the cathepsin only substrate **6QC** and the Casp3 only substrate probe **Casp3-QC** (Fig. 3a). Importantly, the negative control probes produce no visible signals confirming the linker stability observed *in vitro*. Mice were splayed to show localized fluorescent signal within the tumors compared to surrounding fat tissue (Fig. 3b). Quantification of average tumor fluorescence in splayed tumors confirmed that both the **DEATH-CAT 2** and single substrate probe **6QC** produced a significantly increased signal compared to the negative controls **(D)-Phe 2** and **(D)-Asp 2**, and that this level of contrast over controls was several-fold higher for the AND-Gate probe (Fig. 4a). The Casp3-specific substrate probe **Casp3-QC** that has only the caspase half of the AND-Gate substrate showed low-level tumor signal, however it was not significantly higher than the two negative control probes. The tumor-to-background ratio

(TBR) for the **DEATH-CAT 2** was also significantly increased over the single-parameter **6QC** probe (3.0 ± 0.3 compared to 2.3 ± 0.5; Supplementary Fig. 6).

To determine the fluorescence activation in healthy organs compared to tumors, we excised relevant organs for *ex vivo* imaging and quantified fluorescent signal intensities. We found that the fluorescent signals in excised liver, kidneys, and lung tissue was significantly reduced in the animals treated with **DEATH-CAT 2** compared to those treated with **6QC** (Fig. 4c). Quantification of the fold change in fluorescent signals over tumor signals for each tissue confirmed the dramatic increase in selectivity of the AND-Gate probe compared to the cathepsin-only **6QC** probe (Fig. 4d). As a further analysis of probe activation *in vivo*, we fixed and embedded excised tumors for cryo-sectioning and immunofluorescence analysis (Fig. 4b). We stained tumor sections for CD68, a marker for macrophages, as well as for cleaved Casp3. This analysis confirmed the presences of macrophages within the 4T1 breast tumors, as has been previously described[20]. We also observed numerous regions within the tumor tissues where cells contained active Casp3. These regions of apoptotic cells were always found directly adjacent to, or co-localized with, macrophage cell populations. The brightest probe signal was always found at the intersection between macrophages and cells with active Casp3 confirming that Casp3 and Cats are both active within a tumor and generally found in close proximity making them ideal targets for use in the AND-Gate strategy.

Application to fluorescence-guided surgery

To evaluate the performance of our AND-Gate probe strategy during robotic fluorescence-guided surgery, we synthesized an AND-Gate probe containing a fluorophore that has excitation and emission wavelengths compatible with the FDA approved Firefly® detection system on the da Vinci® Xi Surgical System. Currently, the Firefly® fluorescence detection system is specifically tuned to the excitation/emission properties of indocyanine green (ICG, ex/em: 780/820 nm). We initially sought to synthesize an AND-Gate probe containing the conjugatable version of ICG (containing a carboxylic acid) and the respective quencher QC-1, which is non-fluorescent and has strong absorbance between 600–900 nm. However, conjugating ICG to the peptide scaffold caused unexpected issues possibly caused by aggregation or tertiary folding of the molecule. Therefore, we used a heptamethine cyanine fluorophore FNIR-Tag that was designed to resist aggregation and have better water solubility compared to ICG[35]. We conjugated the FNIR dye successfully to the α-amine on the central (D)-Glu linker and subsequently attach two QC-1 quenchers to the lysine side chains to produce **DEATH-CAT-FNIR** (Supplementary Scheme 3). Although this fluorophore has slightly lower excitation/emission maximum wavelengths compared to ICG (765/788 nm), the fluorescence can be detected by the Firefly® detection system, albeit with lower sensitivity compared to ICG. We confirmed that **DEATH-CAT-FNIR** was efficiently processed by CatL and Casp3 using the recombinant proteases in a fluorogenic substrate assay (Supplementary Fig. 10). Like the Cy5 AND-Gate probes, **DEATH-CAT-FNIR** produced a fluorescent signal only after incubation with both proteases, regardless of order of addition.

We evaluated the performance of **DEATH-CAT-FNIR** with the single substrate probes **6QC-ICG** and **6QC-NIR** as positive controls during robotic surgery on mice bearing 4T1 breast tumors. Both single substrate probes were developed in our laboratory and contain either an ICG or Dylight780-B1 (NIR) fluorophore, which are activated by cysteine cathepsin proteases[25]. We injected mice bearing 4T1 breast tumors with probes 2 h prior to performing robotic surgery (20 nmol, I.V.). The **DEATH-CAT-FNIR** produced fluorescent contrast in the tumor compared to the surrounding tissue, which clearly highlighted the margins during surgery (Fig. 5a). Despite using a fluorophore with lower excitation/emission wavelengths compared to ICG, the **DEATH-CAT-FNIR** had comparable fluorescent signal intensity to the **6QC-ICG** probe and much improved signal in comparison to **6QC-NIR**, which also has lower excitation/emission wavelengths than ICG (788/799 nm).

To further demonstrate the utility of the **DEATH-CAT-FNIR** probe, we performed a resection of a primary subcutaneous mammary tumor and subsequently used probe fluorescence to assess the remaining subcutaneous tumor bed (Fig. 5b). The residual cancer cells left after excision of the primary tumor were not visible by white light imaging but could easily be visualized using Firefly® detection of the probe signal (Supplementary Movie 1). We then removed the subcutaneous tumor bed and overlying skin with significant surrounding probe-negative tissue. This tissue was formalin-fixed and sectioned such that hematoxylin and eosin (H&E) slides contained both probe positive and probe negative regions on a single slice. Analysis of the H&E stained tissues by a board-certified pathologist confirmed that the regions showing probe activation contain residual tumor left behind following excision, while probe negative regions contained normal subcutaneous and cutaneous tissue (Fig. 5c, d). Thus, the **DEATH-CAT-FNIR** probe was able to accurately detect areas of residual tumor cells left behind after excision of a bulk tumor.

Following robotic surgery, tumors and organs from mice injected with each probe were imaged *ex vivo* using the LiCor Pearl imaging system to quantify the fluorescent signal. Representative images of excised tumors and organs confirmed a reduced signal in the liver and kidneys compared to the signal found in the tumors for **DEATH-CAT-FNIR,** while both of the 6QC probes showed high background outside of the tumors (Fig. 5e). Quantification of the signal in healthy organs normalized to the tumor signal confirmed a significant reduction in background in the liver for mice injected with **DEATH-CAT-FNIR** compared to both 6QC probes and a significant reduction in background for all healthy organs compared to **6QC-NIR** (Fig. 5f).

AND-Gate probe targeting FAPα and Cathepsins

To demonstrate the generality of the AND-Gate approach for the development of targeted quenched-fluorescent probes, we sought to combine the successful CAT substrate sequence (z-FK) with another protease that is highly expressed in the tumor microenvironment. We chose FAP because it has increased proteolytic activity in a broad range of tumor types and has a unique substrate specificity profile with a strong preference for a Glycine-Proline (GP) sequence[36,37]. We synthesized and evaluated three single substrate FAP probes containing a GP, glycine-proline-asparagine (GPN), and glycine-proline-serine (GPS) amino acid sequence to validate and further optimize a FAP sequence for incorporation into an AND-

Gate probe (Supplementary Fig. 11a). Adding an additional P1' asparagine or serine has been demonstrated to increases specificity for FAP and increase the rate of substrate turnover[38,39,40]. The GPN and GPS sequences containing a sulfo-Cy5/sulfoQSY-21 had approximately a 20-fold increase in initial velocities compared to the GP sequence (Supplementary Fig. 11b). We chose the GPS sequence for incorporation into an AND-Gate probe to increase the solubility of the probe. Attempts to synthesize an AND-Gate probe using the GPN sequence caused issues during the synthesis.

We synthesized an AND-Gate probe containing the cathepsin and FAP sequences, **FAP-CAT** using the same chemistry and linker used for the **DEATH-CAT** probe (Supplementary Scheme 4). The structure of the **FAP-CAT** probe is shown in Fig. 6a and contains a central (D)-Glu linker and a sulfo-Cy5/sulfo-QSY21 fluorophore-quencher system. We confirmed that the **FAP-CAT** probe activates only after incubation with both FAP and CatL in either order but not when individual proteases were used (Supplementary Figure 12). We first tested the FAP-CAT probe in the 4T1 breast tumor model for direct comparison to **6QC** and the single substrate FAP probe **GPS** (For structure of **GPS** probe see Supplementary Fig. 11). Probe signal in splayed 4T1 tumors 4 h post injection (10 nmol, I.V.) confirmed increased fluorescence contrast for the **FAP-CAT** probe compared to the single substrate probes **6QC** and **GPS** (Fig. 6b, for all splayed tumor images see Supplementary Fig. 13). The **FAP-CAT** probe also showed significantly increased overall signal and TBR within 4T1 tumors compared to both single substrate probes (Fig. 6c, d). Interestingly, the signal arising from **FAP-CAT** in splayed tumors was more concentrated on the outer margins of the tumor compared to signal from activated **DEATH-CAT 2**, where the most intense signal was found in the core of the tumor (*vide infra*). Immunofluorescence analysis of FAP expression in sectioned 4T1 tumors confirmed that the probe fluorescence is found at the edge of the tumor and localizes with FAP expression (Fig. 6e). In the core of the tumor, FAP expression is low and so is probe activation, consistent with previous reports that FAP activity is localized at the invasive edges of tumors (Supplementary Fig. 14)[41–43].

Detection of lung cancer metastases with AND-Gate probes

To demonstrate the ability of the probes to detect small metastatic cancer lesions, we further evaluated the AND-Gate probes in a metastatic lung cancer model. Mice were injected with metastatic kras$^{G12D/+}$p53$^{-/-}$ lung adenocarcinoma cells (1×10^5 cells, I.V.), which resulted in seeding and growth of cancer lesions in the lungs[44,45]. Three weeks after seeding of cancer cells, mice were injected with **DEATH-CAT 2** and **FAP-CAT**, and the single substrate probes **6QC** and **GPS** (30 nmol, I.V.). Mice were sacrificed and resected lungs were imaged 16 h post injection (Fig. 7a). Both AND-Gate probes were able to detect lung metastases including those that are less than 1 mm in diameter. The imaged mouse lungs were sectioned, stained for H&E, and evaluated for the presence of lung metastases. The location of fluorescence probe signals corresponded to the location of metastases based on H&E staining (Fig. 7b). In addition, the **DEATH-CAT 2** probe produced a significantly brighter signal compared to **FAP-CAT** and **6QC** (Fig. 7c) and both AND-Gate probes displayed better TBRs than **6QC** when compared to surrounding tissue and lung tissues from healthy mice (Fig. 7d, e). The single substrate FAP probe **GPS** was not able to clearly define lung metastases and was not evaluated further.

Because **DEATH-CAT 2** was the best performing AND-Gate probe for detection of metastatic lung tumors, we assessed the ability of the **DEATH-CAT-FNIR** probe to be used for robotic surgery in this model. We therefore dissected mice bearing metastatic lung tumors 16 h post probe injection using the Da Vinci surgical system (Supplementary Video 2). Screen captures of the recorded dissection demonstrates that the NIR camera system enabled us to detect metastases in the lungs in real time (Fig. 8a, b). We then resected lungs and subsequently imaged the tissues using the LiCor Pearl imaging system (Fig. 8c). This analysis confirmed the probe selectivity for metastatic lesions and matched with the data obtained in real time using the Firefly detector. Finally, to demonstrate the ability of the AND-Gate probe to be used as a diagnostic indicator as well as a real-time optical contrast agent, we fixed and sectioned the resected lungs to confirm that fluorescent hot spots correspond to sites of tumors. Metastatic lesions were clearly visualized by fluorescent signal from the probe in scanned tissue sections and this signal matched the location of tumor cells as determined by adjacent H&E stained slides (Fig. 8d). The **DEATH-CAT-FNIR** probe was able to locate metastatic cancer lesions that were less than 1 mm in diameter using both the robotic surgical system and LiCor imaging system. Furthermore, the fluorescent signal from the probe was able to withstand tissue fixation conditions (4% Paraformaldehyde, PFA) allowing sectioned tissues to be scanned for identification of metastatic lesions as a diagnostic aid.

Discussion

The sensitive and accurate detection of tumor margins and metastases is a central goal for effective treatment of any type of solid tumor during surgery. Currently, there are a number of effective ways to image the location of a tumor in the body. However, most of the current imaging strategies are not suitable for real-time applications during surgery. Furthermore, they often depend on contrast agents that lack a level of specificity needed to be used in diverse cancer tissue types. Recent efforts to address these limitations in current imaging technologies have focused on targeted contrast agents that produce fluorescent signals only within the tumor microenvironment. While this approach has proven valuable and several agents are currently in human clinical trials, there still remains a need to find strategies to improve the selectivity of optical contrast agents so that they can be used in virtually any type of tumor resection. We and others have developed activatable ‘smart probes’ that turn on a fluorescent signal when processed by a protease that is highly activated in tumor tissues. These reagents provide overall high contrast in some tumor types where levels of the active protease in the surrounding normal tissues is low. Here, we outline a general strategy to generate a next-generation of optical smart probes that require the processing by multiple tumor-associated enzymes. This multivariate AND-Gate sensor has the potential for highly increased tumor selectivity by incorporating substrates that are specifically processed by enzymes that exist in normal tissues but that are only found together in the tumor microenvironment. Using this strategy, background signal in healthy surrounding tissue is eliminated, resulting in high image contrast and clear margin detection even for probes with overall low signal strength.

We chose to build the first AND-Gate probe using two substrates cleaved by cysteine cathepsins[20,25] and Casp3[46,47]. We chose this combination of enzymes because of their non-

overlapping primary sequence specificity. Furthermore, while all tissues contain some level of active cathepsins, Casp3 is only activated in the late stages of apoptosis, which typically does not take place in healthy tissues. Multiple types of cell death are activated within tumors as the result of several factors including nutrient and oxygen starvation[32,48,49]. Dying cells within the tumor activate infiltrating immune cells, such as macrophages that then clear the cells by lysosomal engulfment. Therefore, there exists a specific niche within the tumor microenvironment where both lysosomal and apoptotic proteases co-exist, making these proteases ideal choices for use in tumor-specific AND-Gate sensors.

To show the generality of the AND-Gate approach, we combined the general cathepsin substrate with FAP. The FAP protease is another ideal target for an AND-Gate probe because it has increased activity in numerous cancer types and is generally not active in normal tissues[36,37,42]. Additionally, FAP has a unique substrate specificity profile preferring a P1 Pro, which is orthogonal to many other protease sequence preferences[38]. This probe combined two sequences specific for an extracellular protease and lysosomal proteases, which could accumulate within tumors. In comparison, the single substrate probe that targeted only FAP did not accumulate in tumors to the same extent. This suggests that combining a lysosomal protease with an extracellular protease sequence can be a means of achieving activation and accumulation within a tumor for more specific visualization of tumor margins and metastases.

Because we have designed a general strategy in which the fluorescent reporter is attached to a central linker that is the final end product of probe processing, it is possible to further engineer our first generation AND-Gate probes to respond to additional enzymatic processes beyond a binary set of targets. This hub and spoke model should also be amenable to further optimization of chemistry to allow production of diverse AND-Gate sensors by swapping of the spokes around the central fluorescent hub. In addition, it is possible to replace the current quencher/fluorophore strategy with a Förster Resonance Energy Transfer (FRET) fluorophore pair that would allow ratiometric imaging to detect probe distribution as well as activation. This strategy would help to reduce heterogeneity of imaging signals due to differential probe distribution while also reducing background signals by allowing quantification based on a ratio of signals, which can be a large value even when probe concentrations are low. We are currently working to develop ratiometric AND-Gate probes as well as multivariate versions that respond to more than two proteases. There are many additional proteases that have been shown to be preferentially activated in solid tumors of diverse origins, and many of these proteases have defined substrate specificity that would make design of next generation AND-Gate sensors straightforward.

In addition to using the multivariate AND-Gate strategy to improve imaging contrast, it should in theory also be possible to apply this approach for selective drug delivery applications. Such a strategy would require attachment of an individual or multiple drugs to the central hub through linkages that block activity of the agents and that can be processed within a specific tissue location. One could envisage such an AND-Gate therapy that releases one or more active drugs only when multiple proteases cleave the linkages tethering the molecules to one another. We are currently exploring approaches to use the AND-Gate approach for such applications.

We show here that the **DEATH-CAT-FNIR** probe is compatible with existing robotic surgical systems and workflows to enable visualization of residual tumor tissue remaining after removal of a primary mass and small metastases (< 1 mm in diameter). These results suggest that the AND-Gate strategy will enhance the effectiveness of tumor resections during fluorescence-guided surgery even in locations where high background signal would normally limit effective visualization of the margin.

Outlook

Overall, the studies presented here provide a roadmap for the design of optical contrast agents that respond to unique enzymatic signatures that are indicative of a disease state. In the current design, we demonstrate the utility of the AND-Gate approach using substrates that are uniquely processed by two proteases, which are both activated in the tumor microenvironment. The design of the AND-Gate protease probe used here required engineering of the linker group to prevent activation by undesired protease activities found in normal healthy tissues but ultimately resulted in contrast agents that both improve tumor-selectivity and also increase tumor uptake resulting in a brighter overall signal. We are currently working to further optimize the central linker such that higher order probes can be rapidly generated by attachment of various substrates containing quenchers using orthogonal chemistry. This should allow synthesis of probes with high selectivity for diverse cancer types based on proteolytic signatures of those tumors. It also should, in principle, enable generation of probes that respond to other classes of enzymes in diverse disease states that are capable of processing substrates to liberate a central fluorescent or therapeutic fragment.

Methods

Chemistry Methods

The synthesis protocols are provided in the Supplementary Information.

Biology Methods

General Cell Culture—4T1 cells and RAW246.7 macrophages were cultured separately as previously describe[20,50]. RAW246.7 macrophages were cultured in Dulbecco's Modified Eagle's medium (DMEM, Gibco, REF: 11965–092) containing 4.5 g/L of glucose supplemented with 10% fetal bovine serum (FBS, GeminiBio, Cat #: 100602), and 100 units/ml penicillin and 100 μg/mL streptomycin (Pen Strep, Gibco, REF: 15140–122). 4T1 cells were cultured in Roswell Park Memorial Institute (RPMI, Corning, REF: 10–040-CV) 1640 medium containing 2 g/L of glucose, 0.3 g/mL of L-glutamine, and supplemented with 10% FBS, and 100 units/mL penicillin and 100 μg/mL streptomycin. The $kras^{G12D/+}p53^{-/-}$ lung adenocarcinoma cells were cultured in DMEM containing 4.5 g/L of glucose supplemented with 10% fetal bovine serum (FBS), and 100 units/ml penicillin and 100 μg/mL streptomycin.

Fluorogenic Substrate Assay—All proteases were active site titrated as previously described to obtain active protease concentrations[20]. The buffers used for caspases, fibroblast activation protein α, and cathepsins were made as previously described[20,33]. The reducing agent 1,4-dithiothreitol (DTT, VWR, Cat #: 0281) was freshly added to buffers just

prior to use. All assays were conducted in black, opaque flat bottom 384-well plates (Greiner Bio-One, REF: 781076). For single substrate probes and first cleavage of AND-Gate probes, compounds were diluted in the respective protease buffer from 10 mM stock solutions in DMSO (Santa Cruz Biotechnology, Cat. #: sc358801), and 15 μL of substrate (20 μM) was added to each well. Immediately prior to beginning fluorescent measurements, 15 μL of protease was added to wells containing substrate using a multichannel pipette. All proteases were at a final concentration of 10 nM in the well unless otherwise indicated. Fluorescent measurements for probes containing a sulfo-Cy5 were read above the well with a Biotek Cytation3 Imaging Reader (7.00 mm read height, gain = 100, ex/em = 640/670 nm, normal read speed). Fluorescent measurements for probes containing ICG or FNIR-Tag fluorophores were read above the well with a SpectraM2 plate reader (7.00 mm read height, ICG: ex/em 780/820 nm, FNIR-Tag: ex/em 765/790 nm, normal read speed).

After confirming AND-Gate probes are not activated upon single addition of protease, probes were incubated with single proteases in an Eppendorf tube prior to second protease addition and fluorescent measurements. AND-Gate probes or negative controls (40 μM) were initially digested in 20 nM protease in the respective protease buffer. After 2 h at 37 °C, reactions with cathepsin buffer (pH 5.5) were exhausted by addition of 2 M NaOH (1.4 μL/100 μL of buffer) and then diluted with caspase buffer to obtain a concentration of 20 μM total substrate (pH 7.0). Reactions containing caspase buffer (pH 7.0) were exhausted by addition of 1 M HCl (2 μL/100 μL of buffer) followed by dilution with cathepsin buffer to obtain a final concentration of 20 μM total substrate (pH 5.5). The singularly processed probes were added to wells (15 μL) and the second protease was added just prior to beginning fluorescent measurements (15 μL, 10 nM final protease concentration, 10 μM final substrate concentration). Fluorescent signal over time was measured as mentioned above.

Live Cell Fluorescent Microscopy Assay—RAW246.7 macrophages and 4T1 cells were diluted to 1×10^5 cells/mL with their respective media and then mixed in a 1:1 ratio. The mixture of cells were seeded in a 96-well, half-area, μclear® bottom, cell culture plate (Greiner Bio-One, Cat #: 675096) at 30 μL per well, and allowed to adhere to the bottom of the plate for 24 h. Next, cells were incubated with DMSO (1 % v/v) or etoposide (5 μM). After 24h with DMSO or etoposide (Sigma-Aldrich, Cat #: E1383), probes were added to the cell media (5 μL, 1 μM) and incubated for 2 h. Then, Hoescht 33342 (Invitrogen, Cat #: H3570) was added to the media (5 μg/mL) and the cells were imaged using a 40X oil emersion objective on a Zeiss Axiovert 200 M confocal microscope. Acquired Z-stacks consisted of 24 16-bit images taken in 1 μm increments apart beginning and ending 12 μm from the focal plane. The channels used were set on separate tracks. The channel settings were as follows: Cy5-Gain = 545, laser ex = 639 nm, 2% power, Hoescht 33342-gain = 750, laser ex = 405 nm, 4% power, and differential interference contrast (DIC), T-PMT from Cy5 channel, gain = 480.

Images were processed using ImageJ (v1.52p, Rasband, W.S., ImageJ, U.S. National Institutes of Health, Bethesda, Maryland, USA, http://imagej.nih.gov.stanford.idm.oclc.org/ij/, 1997–2011). Zeis image files (.csi) were opened using the Bio-Formats plug-in. Images shown are flattened from Z-stacks by taking the

maximum intensity in each pixel using the Z projection function. All images are adjusted to the same contrast and brightness levels. The corrected total cellular fluorescence (CTCF) was determined by manually tracing cells using the Region of Interest Manager function (ROI Manager) based on the DIC and nuclear staining images, and measuring the total fluorescence within each cell from the flattened Z-stack images. CTCF was calculated according to the following formula: CTCF = Integrated density – (area of cell x average background). The average background was obtained by tracing circles where no cells were present and averaging the overall signal. Cells that were overlapping or on the edge of the image were not counted. CTCF measurements were normalized to **DEATH-CAT 2**, DMSO treated control to obtain fold-change values.

Animal Models and Fluorescent Imaging—All experiments involving animals were approved and conducted in accordance with current National Institutes of Health and Stanford University Institutional Animal Care and Use Committee guidelines. All animals were kept in a Stanford University Medical School housing facility in a climate-controlled room (23 ºC, 40–60% humidity) with a 12 h light/12 h dark cycle. All *in vivo* and *ex vivo* imaging was conducted with a LiCor Pearl Trilogy imaging system. The three excitation/filter sets used for imaging include the 700 nm, 800 nm, and white light channels (Resolution: 85 or 175 μm, Focus Setting: Zero). All displayed images were normalized across experimental cohorts and scales bars are in relative, arbitrary fluorescence units. Scanned unstained sections of tissue were imaged using a LiCor Odyssey CLx flatbed scanner (excitation/filter setting: 800 nM, Resolution: 21 μm, quality set to 'high'). Live mice were imaged at indicated time points after I.V. tail vein injection of probe under isoflurane anesthesia (Fluriso™, NDC: 13985–528-60). Anesthesia was delivered into a nose cone or sealed chamber using a small animal isoflurane vaporizer (VetEquip, Inc., Serial #: VE6780) with induction at 3%, and maintenance at 2% isoflurane flow with oxygen as the carrier. All fluorescent signals were normalized using ImageStudioLite (LiCor, v5.2). For quantitative analysis of fluorescence signal, signal within an ellipsoid region of interest (ROI) surrounding the tumor or metastases was used to calculate the average fluorescence pixel intensity. For TBR calculations, the average signal for each tumor or metastases was divided by the average signal of directly adjacent healthy tissue using the same size ROI.

For *ex vivo* analysis, mice were sacrificed under isoflurane anesthesia by cervical dislocation after *in vivo* imaging was completed. Average fluorescence intensity was measured in each organ by placing an ellipsoid ROI encompassing the organ and normalizing each average intensity to the average fluorescence intensity in the tumors.

4T1 Breast Tumor Model—4T1 cells suspended in 1X phosphate buffered saline (PBS, 100 μL, 1×10^6 cells/mL) were injected subcutaneously into the 3 and 8 mammary fat pads of 6–8 week old BALB/c ByJ female mice (Jackson Laboratory). Mice were monitored for tumor formation and were injected with probe for imaging between 7–10 days after seeding 4T1 cells. Probes were dissolved in 1X PBS (10% DMSO) and injected I.V. tail vein (100 μL, 10 or 20 nmol) using a 1 mL insulin syringe (BD biosciences, 28G). Hair was removed

to expose the tumors with Nair® lotion while the mice were under anesthesia 1 h prior to imaging.

Histological Analysis of 4T1 Tumor Sections using Confocal Fluorescence Microscopy—4T1 breast tumors in the mammary fat pads of BALB/c mice injected with probe were excised postmortem. The tumor tissues were fixed in neutral buffered formalin solution (4% formaldehyde, Sigma-Aldrich, Cat #: HT501128) for 24 h at 4 °C. The fixed tumor tissues were then soaked in 30% w/v sucrose (RPI, Cat #: S24065) in 1X PBS for 24 h at 4 °C. Tumor samples were embedded in Optimal Cutting Temperature (O.C.T.) compound (Tissue-Tek, REF: 4583) and kept at −80 °C until further use. Embedded tissues were then crysosectioned (5–10 μm) onto glass slides. The samples were stored at −20 °C prior to staining. The cryosections were first washed with 1X PBS 3X in a slide chamber. Then, the samples were blocked with 3% w/v BSA (Fisher Scientific, Cat #: BP1600) for 24 h at 4 °C. Samples were washed 3X with 0.5% w/v BSA, then tissues were outlined with a hydrophobic pen, followed by incubation with 1:2,500 dilution of primary antibodies for CD68 (rat anti-mouse, Bio-Rad), cleaved Casp3 (rabbit anti-mouse, Cell Signaling), or FAP (rabbit anti-mouse, R&D Systems) in 0.5% w/v BSA in 1X PBS for 24 h at 4 °C. Samples were then washed 5X with 0.5% w/v BSA in 1X PBS. Tissues were then incubated with anti-rat alexafluor488 and anti-rabbit alexafluor594 secondary antibodies (Invitrogen) diluted 1:5,000 for 1 h at RT. Tissues were washed 5X with 0.5% w/v BSA in 1X PBS, followed by 3X washes with 1X PBS. Tissues were mounted with Vectashield mounting medium containing DAPI (Novus Biologicals, Cat. #: H-1200-NB).

Sections of tumors were imaged using a 40x oil emersion objective on a Zeiss Axiovert 200 M confocal microscope. Images are of a single focal plane (16-bit). All channels were set on separate tracks for imaging. The channel settings were as follows: Cy5–Gain = 730, laser ex = 639 nm, 20% power; A594(cleaved Casp3)–gain = 600, laser ex = 555 nm, 4% power; A488(CD68)–gain = 640, laser ex = 488, 4% power; DAPI–gain = 600, laser ex = 405 nm, 2% power. Additional details about the primary and secondary antibodies used can be found in the Reporting Summary.

Lung Metastases Mouse Model—Male B6129SF1/J mice (8–10 weeks old, Jackson Laboratory) were injected with 1×10^5 $kras^{G12D/+}p53^{-/-}$ lung adenocarcinoma cells (I.V. tail vein, 200 uL) suspended in 1X PBS. Mice bearing lung metastases or healthy mice were injected with probes 21–23 days after initial cancer cell injections (I.V. tail vein, 100 μL). Probes were diluted in 30% v/v PEG400 (Hampton Research, Cat #: HR2–603), 10% v/v DMSO in 1X PBS. Mice were sacrificed and their lungs were resected for imaging.

Robotic Fluorescence-Guided Surgery—Breast tumor-bearing mice (4T1) or mice with lung metastases were administered the indicated probes via I.V. tail vein (100 μL, 20 nmol in 30% v/v PEG400, 10% v/v DMSO in 1X PBS) 2 h prior to surgery. Robotic fluorescence-guided surgery was performed with an FDA approved da Vinci® Xi Surgical System equipped with a Firefly® fluorescence detector. Surgery on breast tumor-bearing mice was initially performed under inhaled isoflurane using the same vaporizer delivery system and method as mentioned in the Animal Models and Fluorescent Imaging section. For pre-surgical pain relief, buprenorphine (0.05 mg/kg) was administered intraperitoneal

(I.P.) while under inhaled anesthesia. After resection of the tumors, mice were put in deep sedation with ketamine/xylazine solution (80 mg/kg ketamine, 10 mg/kg xylazine I.P.), followed by cervical dislocation. Mice bearing lung metastases were sacrificed in the same manner prior to fluorescence-guided surgery to avoid undue pain during the exploratory dissection. Imaging after sacrifice and excision of the lungs was necessary because the fluorescence output is not observable below the peritoneum during live animal imaging. Sacrificing the animal does not affect the fluorescence output of the probes. Breast cancers and lung metastases were detected with a combination of white light and fluorescence signal based on probe activation as a guide to determine tumor margins from healthy tissue. Videos of the surgical procedures are available in the Supporting Information.

Histopathological analysis of 4T1 tumors—Tissues including the bulk 4T1 breast tumor and tissue adjacent to the tumor were excised, fixed in 4% formaldehyde in buffered solution, processed routinely, sectioned at 5–10 μm, and stained for H&E. Adjacent subcutaneous and cutaneous tissues were embedded in paraffin with the subcutaneous side down (bulk tumor adjacent), such that each slide contained both probe-positive and probe-negative regions. Step sections were taken through the entirety of the tissue at 100 μm intervals.

Histopathological analysis of lung metastases—After robotic surgery and/or imaging, resected lungs bearing metastases were fixed in 4% formaldehyde in buffered solution for 24 h at 4 °C. Tissues were then soaked in 30% w/v sucrose in 1X PBS for 24 h. Lungs were embedded in O.C.T. compound and step sectioned at 10 μm through the tissue at 100–200 μm increments. Sections were H&E stained and evaluated for the presence of lung metastases and correlated to fluorescent signals. For mice injected with **DEATH-CAT-FNIR**, unstained lung sections were imaged using a LiCor Odyssey CLx flatbed scanner and adjacent sections were H&E stained for comparison.

Reporting summary

Further information on research design is available in the Nature Research Reporting Summary linked to this article.

Data availability

All data and information necessary to reproduce the results reported in this manuscript are provided. Any additional data that support the findings of this study is available upon reasonable request.

Supplementary Material

Refer to Web version on PubMed Central for supplementary material.

Acknowledgements

This work was supported by NIH grants R01 EB026285 (to M.B.) and Stanford Cancer Institute Translational Oncology Program seed grant (to M.B.), American Cancer Society-Grand View League Research Funding Initiative Postdoctoral Fellowship, PF-19-105-01-CCE (to J.W.), DFG Research Fellowship TH2139/1-1 (to M.T.), and Stanford ChEM-H Chemistry/Biology Interface Predoctoral Training Program and NSF Graduate Research

Fellowship Grant DGE-114747 (to J.J.Y). Special thanks to Scott Snipas in the Guy Salvesen Lab at Sanford Burnham Prebys Medical Discovery Institute for gifting the recombinant caspases used in this study. Thanks to the Turk Lab at J. Stefan Institute for providing the recombinant cathepsin proteases used in this study. Thanks to Stacy A. Malaker and Nick Riley in the Carolyn Bertozzi Lab at Stanford University for the high-resolution mass analysis of the AND-Gate probes. Thanks to Michael P. Luciano and Martin J. Schnermann at the National Cancer Institute for supplying the FNIR-Tag-OSu used to synthesize the **DEATH-CAT-FNIR** probe. Thanks to the Peter Santa Maria Lab for using their SpectraM2 plate reader. Thanks to the Monte Winslow Lab for providing the $kras^{G12D/+}p53^{-/-}$ lung adenocarcinoma cell line used in the lung metastases model. Tissue sectioning and H&E staining was carried out by the Stanford Animal Histology Services (AHS).

Competing interests

J. Sorger, A. Klaassen and A. Antaris are employees of and shareholders of Intuitive Surgical, Inc., which makes the da Vinci Robotic Surgery System used in this study. M. Bogyo has received funding from Intuitive Surgical Inc. for work unrelated to the studies presented in this manuscript and does not hold stock or any advisory/consulting position with the company.

References

1. Tringale KR, Pang J & Nguyen QT Image-guided surgery in cancer: A strategy to reduce incidence of positive surgical margins. Wiley Interdiscip Rev Syst Biol Med 10, e1412 (2018). [PubMed: 29474004]
2. Orosco RK et al. Positive Surgical Margins in the 10 Most Common Solid Cancers. Sci Rep 8, 5686 (2018). [PubMed: 29632347]
3. Yossepowitch O et al. Positive surgical margins after radical prostatectomy: a systematic review and contemporary update. Eur Urol 65, 303–313 (2014). [PubMed: 23932439]
4. Winter JM et al. 1423 pancreaticoduodenectomies for pancreatic cancer: A single-institution experience. J Gastrointest Surg 10, 1199–1210; discussion 1210–1191 (2006). [PubMed: 17114007]
5. McGirt MJ et al. Extent of surgical resection is independently associated with survival in patients with hemispheric infiltrating low-grade gliomas. Neurosurgery 63, 700–707; author reply 707–708 (2008). [PubMed: 18981880]
6. Brouwer de Koning SG, Vrancken Peeters M, Jozwiak K, Bhairosing PA & Ruers TJM Tumor Resection Margin Definitions in Breast-Conserving Surgery: Systematic Review and Meta-analysis of the Current Literature. Clin Breast Cancer (2018).
7. Morrow M et al. Trends in Reoperation After Initial Lumpectomy for Breast Cancer: Addressing Overtreatment in Surgical Management. JAMA Oncol (2017).
8. Weissleder R & Pittet MJ Imaging in the era of molecular oncology. Nature 452, 580–589 (2008). [PubMed: 18385732]
9. Valdes PA, Roberts DW, Lu FK & Golby A Optical technologies for intraoperative neurosurgical guidance. Neurosurg Focus 40, E8 (2016).
10. Zhang J et al. Nondestructive tissue analysis for ex vivo and in vivo cancer diagnosis using a handheld mass spectrometry system. Sci Transl Med 9 (2017).
11. Thill M MarginProbe: intraoperative margin assessment during breast conserving surgery by using radiofrequency spectroscopy. Expert Rev Med Devices 10, 301–315 (2013). [PubMed: 23668703]
12. Garland M, Yim JJ & Bogyo M A Bright Future for Precision Medicine: Advances in Fluorescent Chemical Probe Design and Their Clinical Application. Cell Chem Biol 23, 122–136 (2016). [PubMed: 26933740]
13. Gossedge G, Vallance A & Jayne D Diverse applications for near infra-red intraoperative imaging. Colorectal Dis 17 Suppl 3, 7–11 (2015).
14. Ferraro N et al. The role of 5-aminolevulinic acid in brain tumor surgery: a systematic review. Neurosurg Rev 39, 545–555 (2016). [PubMed: 26815631]
15. Nguyen QT & Tsien RY Fluorescence-guided surgery with live molecular navigation--a new cutting edge. Nat Rev Cancer 13, 653–662 (2013). [PubMed: 23924645]
16. Weissleder R, Tung CH, Mahmood U & Bogdanov A Jr. In vivo imaging of tumors with protease-activated near-infrared fluorescent probes. Nat Biotechnol 17, 375–378 (1999). [PubMed: 10207887]

17. Whitley MJ et al. A mouse-human phase 1 co-clinical trial of a protease-activated fluorescent probe for imaging cancer. Sci Transl Med 8, 320ra324 (2016).
18. Whitney M et al. Ratiometric activatable cell-penetrating peptides provide rapid in vivo readout of thrombin activation. Angew Chem Int Ed Engl 52, 325–330 (2013). [PubMed: 23080482]
19. Sakabe M et al. Rational design of highly sensitive fluorescence probes for protease and glycosidase based on precisely controlled spirocyclization. J Am Chem Soc 135, 409–414 (2013). [PubMed: 23205758]
20. Ofori LO et al. Design of Protease Activated Optical Contrast Agents That Exploit a Latent Lysosomotropic Effect for Use in Fluorescence-Guided Surgery. ACS Chem Biol 10, 1977–1988 (2015). [PubMed: 26039341]
21. Egeblad M & Werb Z New functions for the matrix metalloproteinases in cancer progression. Nat Rev Cancer 2, 161–174 (2002). [PubMed: 11990853]
22. Parks WC, Wilson CL & Lopez-Boado YS Matrix metalloproteinases as modulators of inflammation and innate immunity. Nat Rev Immunol 4, 617–629 (2004). [PubMed: 15286728]
23. Mohamed MM & Sloane BF Cysteine cathepsins: multifunctional enzymes in cancer. Nat Rev Cancer 6, 764–775 (2006). [PubMed: 16990854]
24. Aggarwal N & Sloane BF Cathepsin B: multiple roles in cancer. Proteomics Clin Appl 8, 427–437 (2014). [PubMed: 24677670]
25. Yim JJ, Tholen M, Klaassen A, Sorger J & Bogyo M Optimization of a Protease Activated Probe for Optical Surgical Navigation. Mol Pharm 15, 750–758 (2018). [PubMed: 29172524]
26. Erbas-Cakmak S et al. Molecular logic gates: the past, present and future. Chem Soc Rev 47, 2228–2248 (2018). [PubMed: 29493684]
27. Stennicke HR, Renatus M, Meldal M & Salvesen GS Internally quenched fluorescent peptide substrates disclose the subsite preferences of human caspases 1, 3, 6, 7 and 8. Biochem J 350 Pt 2, 563–568 (2000). [PubMed: 10947972]
28. Blum G et al. Dynamic imaging of protease activity with fluorescently quenched activity-based probes. Nature chemical biology 1, 203–209 (2005). [PubMed: 16408036]
29. Gajewski TF, Schreiber H & Fu YX Innate and adaptive immune cells in the tumor microenvironment. Nat Immunol 14, 1014–1022 (2013). [PubMed: 24048123]
30. Loser R & Pietzsch J Cysteine cathepsins: their role in tumor progression and recent trends in the development of imaging probes. Front Chem 3, 37 (2015). [PubMed: 26157794]
31. Olson OC & Joyce JA Cysteine cathepsin proteases: regulators of cancer progression and therapeutic response. Nat Rev Cancer 15, 712–729 (2015). [PubMed: 26597527]
32. Nikoletopoulou V, Markaki M, Palikaras K & Tavernarakis N Crosstalk between apoptosis, necrosis and autophagy. Biochim Biophys Acta 1833, 3448–3459 (2013). [PubMed: 23770045]
33. Edgington-Mitchell LE & Bogyo M Detection of Active Caspases During Apoptosis Using Fluorescent Activity-Based Probes. Methods Mol Biol 1419, 27–39 (2016). [PubMed: 27108429]
34. Ye D et al. Bioorthogonal cyclization-mediated in situ self-assembly of small-molecule probes for imaging caspase activity in vivo. Nat Chem 6, 519–526 (2014). [PubMed: 24848238]
35. Luciano MP et al. A Nonaggregating Heptamethine Cyanine for Building Brighter Labeled Biomolecules. ACS Chem Biol 14, 934–940 (2019). [PubMed: 31030512]
36. Busek P, Mateu R, Zubal M, Kotackova L & Sedo A Targeting fibroblast activation protein in cancer - Prospects and caveats. Frontiers in bioscience 23, 1933–1968 (2018).
37. Pure E & Blomberg R Pro-tumorigenic roles of fibroblast activation protein in cancer: back to the basics. Oncogene 37, 4343–4357 (2018). [PubMed: 29720723]
38. Edosada CY et al. Peptide substrate profiling defines fibroblast activation protein as an endopeptidase of strict Gly(2)-Pro(1)-cleaving specificity. Febs Lett 580, 1581–1586 (2006). [PubMed: 16480718]
39. Bainbridge TW et al. Selective Homogeneous Assay for Circulating Endopeptidase Fibroblast Activation Protein (FAP). Sci Rep-Uk 7 (2017).
40. Zhang HE et al. Identification of Novel Natural Substrates of Fibroblast Activation Protein-alpha by Differential Degradomics and Proteomics. Mol Cell Proteomics 18, 65–85 (2019). [PubMed: 30257879]

41. Hua X, Yu L, Huang X, Liao Z & Xian Q Expression and role of fibroblast activation protein-alpha in microinvasive breast carcinoma. Diagnostic pathology 6, 111 (2011). [PubMed: 22067528]
42. Zi F et al. Fibroblast activation protein alpha in tumor microenvironment: recent progression and implications (review). Molecular medicine reports 11, 3203–3211 (2015). [PubMed: 25593080]
43. Fang J et al. A potent immunotoxin targeting fibroblast activation protein for treatment of breast cancer in mice. International journal of cancer 138, 1013–1023 (2016). [PubMed: 26334777]
44. Winslow MM et al. Suppression of lung adenocarcinoma progression by Nkx2–1. Nature 473, 101–104 (2011). [PubMed: 21471965]
45. DuPage M et al. Endogenous T cell responses to antigens expressed in lung adenocarcinomas delay malignant tumor progression. Cancer cell 19, 72–85 (2011). [PubMed: 21251614]
46. Vickers CJ, Gonzalez-Paez GE & Wolan DW Discovery of a highly selective caspase-3 substrate for imaging live cells. ACS Chem Biol 9, 2199–2203 (2014). [PubMed: 25133295]
47. Julien O et al. Quantitative MS-based enzymology of caspases reveals distinct protein substrate specificities, hierarchies, and cellular roles. P Natl Acad Sci USA 113, E2001–E2010 (2016).
48. Jaattela M Multiple cell death pathways as regulators of tumour initiation and progression. Oncogene 23, 2746–2756 (2004). [PubMed: 15077138]
49. Labi V & Erlacher M How cell death shapes cancer. Cell death & disease 6, e1675 (2015). [PubMed: 25741600]
50. Verdoes M et al. Improved quenched fluorescent probe for imaging of cysteine cathepsin activity. J Am Chem Soc 135, 14726–14730 (2013). [PubMed: 23971698]

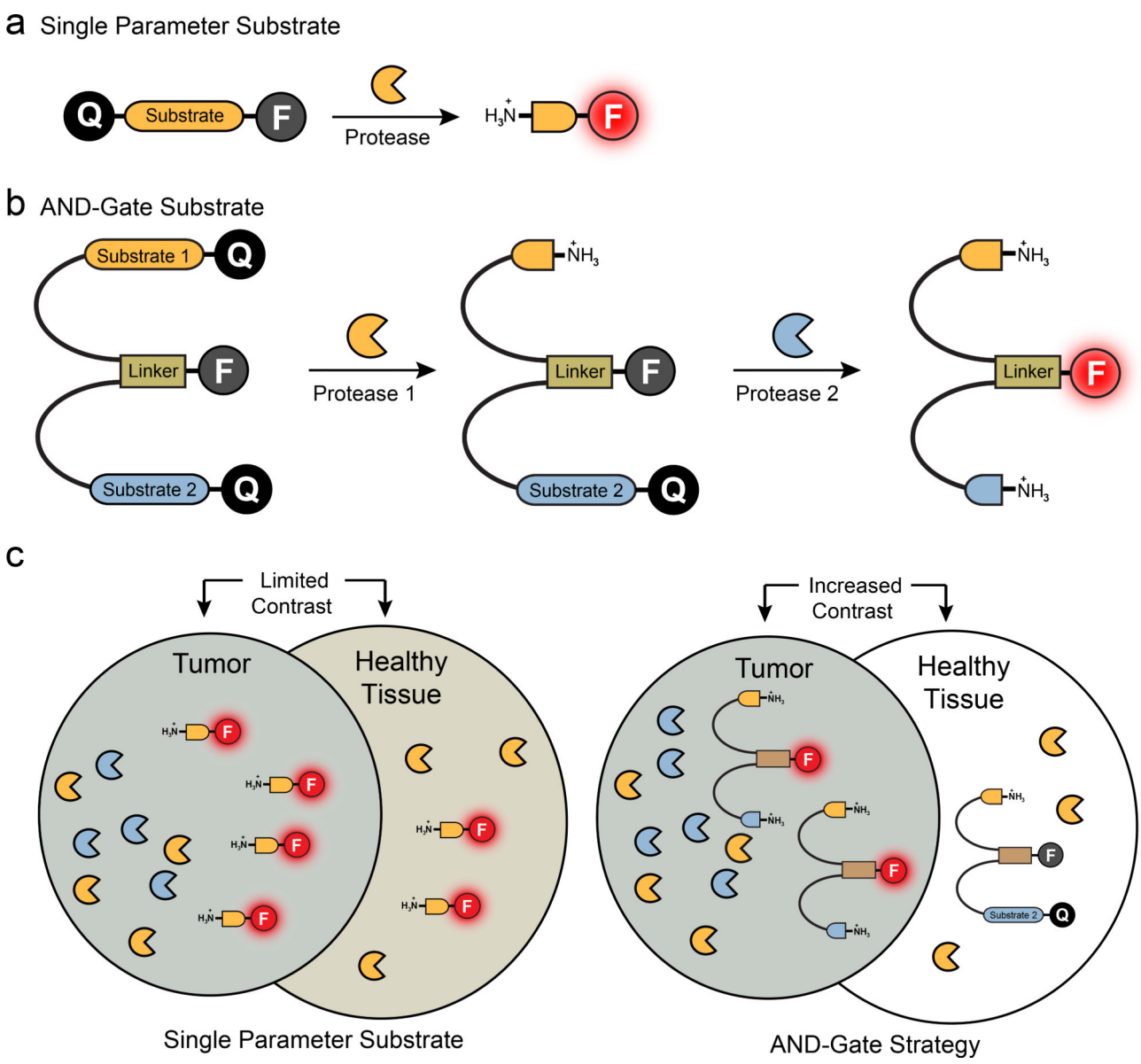

Fig. 1 |. The AND-Gate strategy.

a, Schematic of a single-parameter quenched-fluorescent protease substrate that is cleaved by a single protease to produce a fluorescent fragment. These probes take advantage of higher proteolytic activity in tumors to generate contrast. **b**, Schematic of the multivariate AND-Gate probe, which requires two proteolytic processing events to activate fluorescence. **c**, Comparison of the single-parameter and AND-Gate probes in tumor and normal tissues. Higher contrast is generated by the AND-Gate probe due to lack of activation in normal tissues which lack both protease activities.

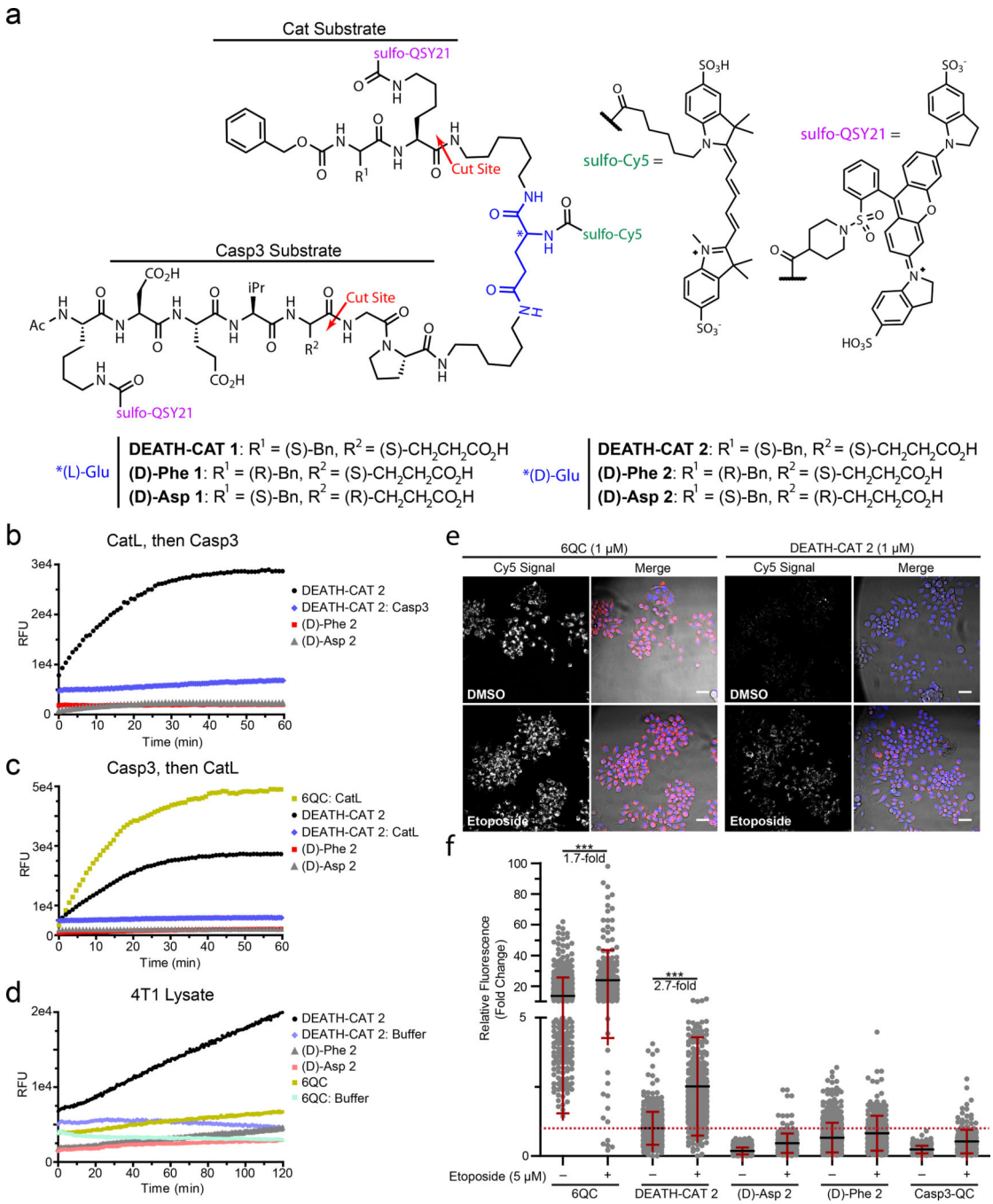

Fig. 2 |. Structure and *in vitro* validation of AND-Gate probes.

a, Structures of the dual orthogonal protease substrate AND-Gate probes and corresponding negative controls. **DEATH-CAT 1** contains the natural amino acid (L)-Glu while the **DEATH-CAT 2** contains a non-natural (D)-Glu linker (blue). The negative control probes contain either a (D)-Asp in the P1 position of the Casp3 sequence (**(D)-Asp 1**) or (D)-Phe in the P2 position of the Cat sequence (**(D)-Phe 1**) to block proteolytic cleavage by the respective protease. **b**, Progress curve of **DEATH-CAT 2** incubated with CatL followed by Casp3 compared to negative control probes **(D)-Phe 2** and **(D)-Asp 2** and with Casp3 only

(10 nM). All substrates were used at 10 μM. **c**, Progress curves as in (**b**) except Casp3 was added first followed by CatL. The single substrate probe **6QC** was incubated with CatL alone. **d**, Progress curve over 2 hours incubation of **DEATH-CAT 2** compared to **6QC** and corresponding negative controls, **(D)-Phe-2** and **(D)-Asp-2**, in either buffer or tumor lysate generated from 4T1 breast tumors in BALB/c mice. **e**, Representative fluorescent microscopy images of 4T1 cells co-cultured with RAW macrophages (1:1 ratio) labeled with either the single-parameter cathepsin probe **6QC** or the **DEATH-CAT 2** probe. Cells were incubated with either DMSO or etoposide (5 μM) for 24 h prior to addition of probes (1 μM). After 2 h, Hoechst stain was added to visualize nuclei and the cells were imaged. The Cy5 signal is shown in gray scale in the left panels. For merged images on the right, brightfield is in grayscale, blue is nuclear staining, and red is the Cy5 probe signal. Representative images of the negative controls **(D)Phe 2**, **(D)Asp 2**, and **Casp3-QC** can be found in the Supplementary Information. Scale bars are 20 μm. **f**, Scatter plot of fluorescent signal from (**e**) shown as the fold change of corrected total cellular fluorescence normalized to cells incubated with DMSO and the **DEATH-CAT 2** probe (Mann-Whitney Test, two-tailed: *** $p < 0.0001$). Sample mean ± S.D., sample size (n) are as follows–**6QC**(DMSO): 13.6 ± 12.1, 416; **6QC**(Etoposide): 23.9 ± 19.6, 266; **DEATH-CAT 2**(DMSO): 1.0 ± 0.6, 398; **DEATH-CAT 2**(Etoposide): 2.7 ± 1.8, 462; **(D)-Asp 2**(DMSO): 0.7 ± 0.5, 599; **(D)-Asp 2**(Etoposide): 0.8 ± 0.6, 246; **(D)-Phe 2**(DMSO): 0.2 ± 0.1, 402; **(D)-Phe 2**(Etoposide): 0.5 ± 0.4, 269; **Casp3-QC**(DMSO): 0.2 ± 0.1, 226; **Casp3-QC**(Etoposide): 0.5 ± 0.4, 205. The data presented were acquired from three biological replicates. Total images taken for each condition includes three field of views per well from six separate wells.

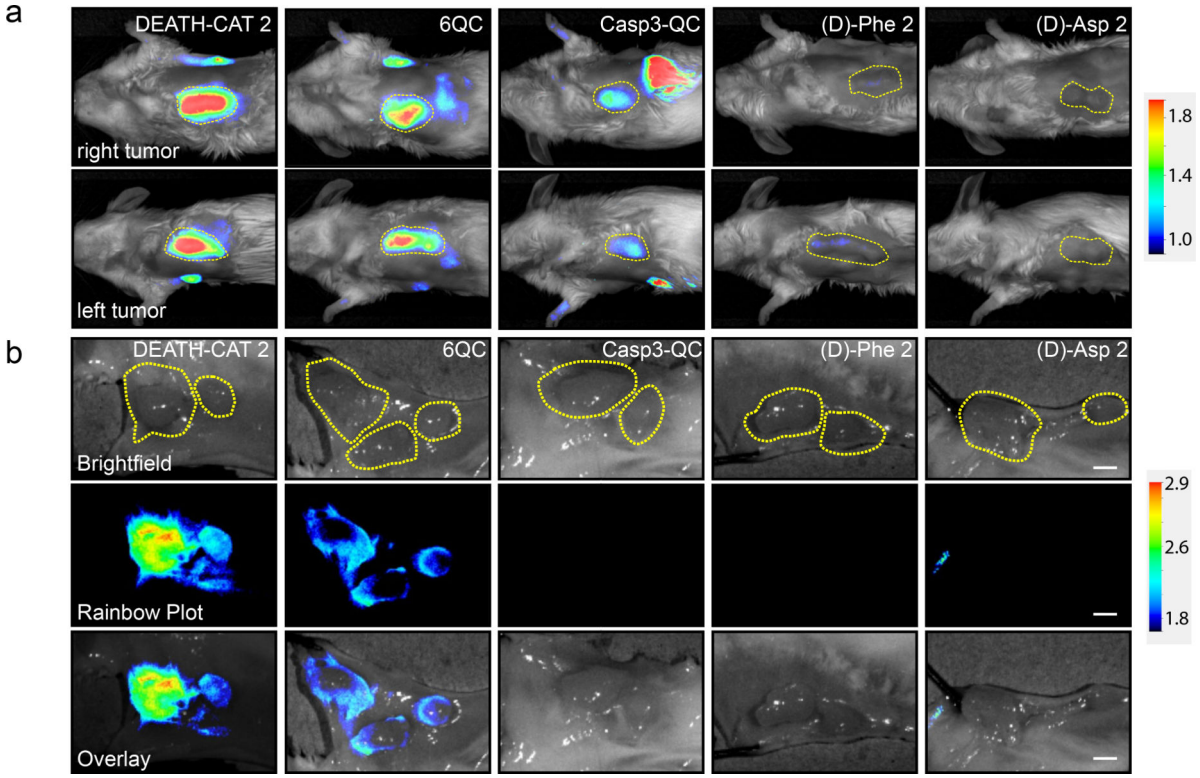

Fig. 3 |. Enhanced selectivity and sensitivity of DEATH-CAT 2 in the 4T1 breast tumor model.
a, Images of live mice bearing 4T1 breast tumors 2 hr after probe injection (20 nmol, I.V.). **b**, Representative images of splayed 4T1 tumors 2 h post injection. Fluorescent signal in tumors in live and splayed mice are displayed as rainbow plots and are normalized across representative images from each cohort. Tumor outlines are indicated with yellow dotted lines. Scale bars = 3 mm. Representative images are presented were acquired from at least 10 biological replicates. All images of live mice bearing 4T1 breast tumors from this study can be found in the Supplementary Information.

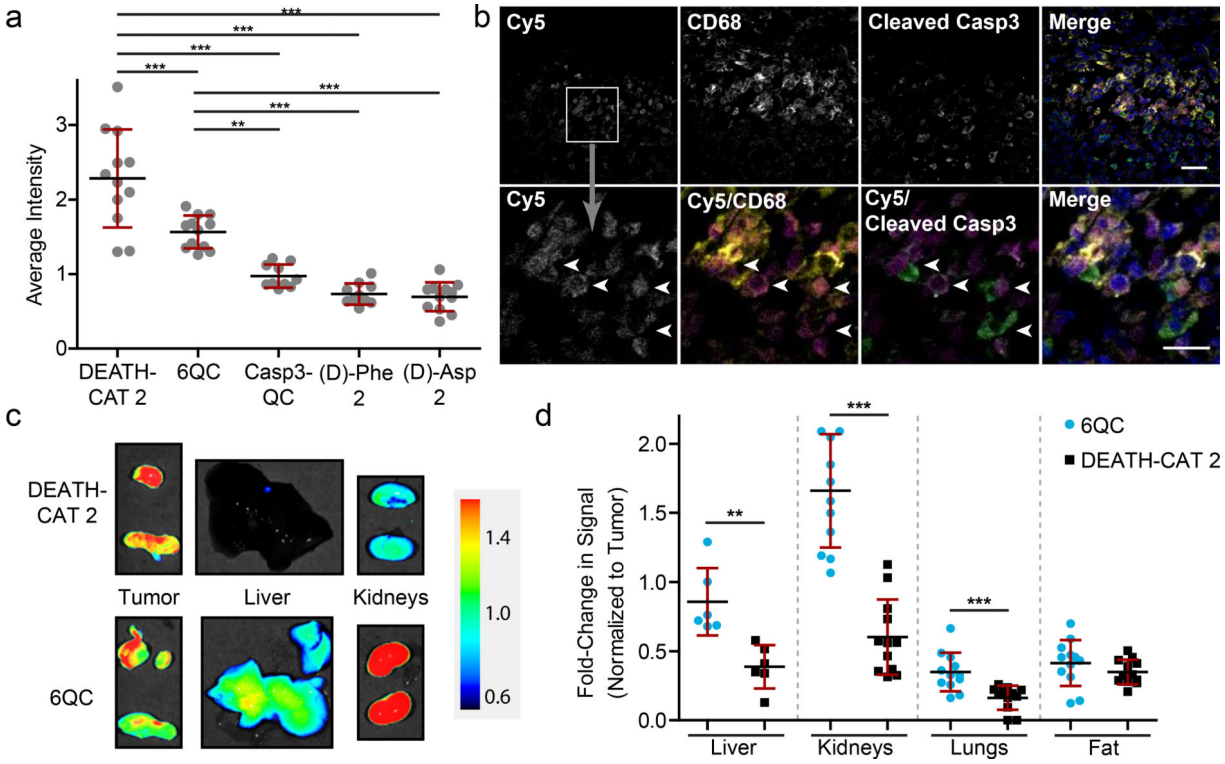

Fig. 4 |. Quantitative analysis of DEATH-CAT 2 compared to single substrates and negative controls in the 4T1 breast tumor model.

a, Scatter plot of average fluorescent signal within splayed tumors from all mice 2 h post injection of each probe (20 nmol, I.V.). (One-way ANOVA, Tukey's Multiple Comparison Test, multiplicity adjusted p-values: **p = 0.002, ***p < 0.0001). Sample mean ± S.D., sample size (n) are as follows–**DEATH-CAT 2**: 2.3 ± 0.7, 12; **6QC**: 1.6 ± 0.2, 12; **Casp3-QC**: 1.0 ± 0.2, 10; **(D)-Phe 2**: 0.7 ± 0.1, 10; **(D)-Asp 2**: 0.7 ± 0.2, 12. **b**, Immunofluorescence microscopy images of 4T1 tumor sections from mice treated with **DEATH-CAT 2** and stained for cleaved Casp3 and CD68 using specific antibodies. Single channel images are in grayscale. Merge images are as follows: Cy5 (probe) is magenta, CD68 is yellow, cleaved Casp3 is green, DAPI is blue. The same contrast and brightness settings were used to process each image. Top column images scale bar is 50 μm and lower column scale bar is 10 μm. Images of additional examples of stained 4T1 tumor sections can be found in the Supplemental Information and are representative of fifty field of views. **c**, Images of excised organs of mice (2 h post injection). Fluorescent signal is displayed as rainbow plots and is normalized between images. Images are representative of each cohort. **d**, Scatter plot of the fold change in fluorescence signal compared to tumor signals for each tissue type in mice treated with the indicated probes. (Student's T-test, two-tailed, Benforroni-Holm Procedure, unadjusted p-values: **p = 0.01, ***p < 0.001). Sample mean ± S.D., sample size (n) are as follows–**6QC**(liver): 0.9 ± 0.2, 6; **DEATH-CAT 2**(liver): 0.4 ± 0.2, 6; **6QC**(kidneys): 1.7 ± 0.4, 12; **DEATH-CAT 2**(kidneys): 0.6 ± 0.3, 12; **6QC**(lungs): 0.3 ± 0.1, 12; **DEATH-CAT 2**(lungs): 0.2 ± 0.1, 12; **6QC**(fat): 0.4 ± 0.2, 12; **DEATH-CAT 2**(fat): 0.3 ± 0.1, 12. Overlay images of fluorescent signal and brightfield of all live mice,

splayed tumors, and excised organs from each cohort can be found in the Supplementary Information. The data presented were acquired from at least 10 biological replicates.

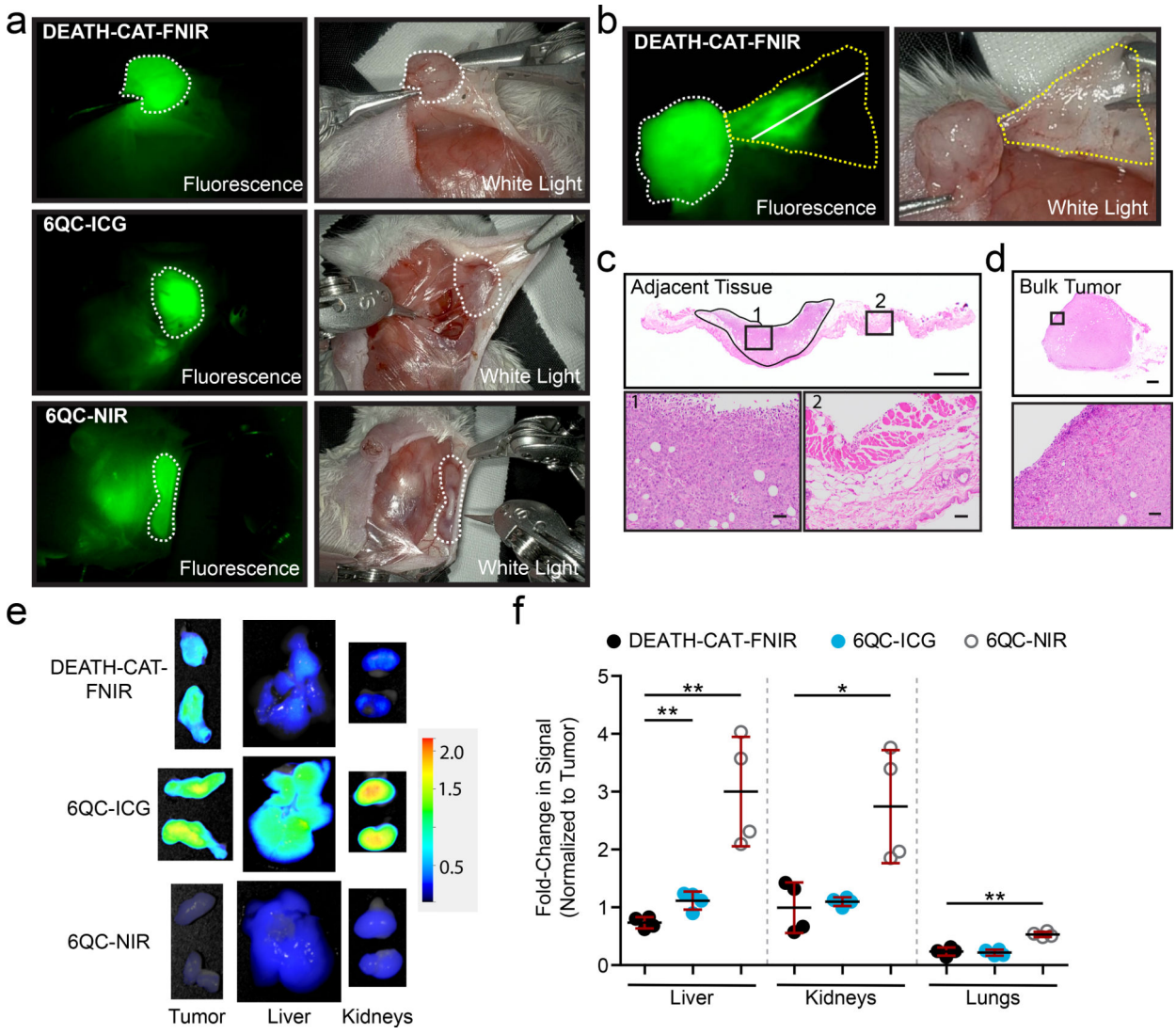

Fig. 5 |. Images from robotic fluorescence-guided surgery and quantification of fluorescence signal in healthy organs.

a, Screen captures of fluorescence signal and brightfield views during dissection of 4T1 breast tumors in mice injected with **AND-Gate-FNIR**, **6QC-ICG**, or **6QC-NIR** (20 nmol, I.V.). Tumors are outlined with white dotted line. **b**, Screen capture images (fluorescence and white light) of a primary excised tumor (white dotted line) and the resulting adjacent tissue (yellow dotted line). The remaining tumor bed (including the subcutaneous and cutaneous tissue) was excised for sectioning. Histology was performed on sections of the tumor bed (solid white line indicating position of histology section) and the bulk tumor. Sectioning was performed perpendicular to the plane of the image. **c**, H&E staining of adjacent probe-positive and probe-negative tissue (scale bar = 500 μm) with images of regions of residual tumor (area 1, scale bar = 50 μm) and surrounding healthy tissue (area 2, scale bar = 50 μm). The black outline indicates area of tumor within the section. Images are representative of ten stepwise sections through the tissue. **d**, H&E staining of a section taken from the bulk tumor (scale bar = 500 μm) and a zoomed in region shown in the box area

(scale bar = 50 μm). **e**, Representative images of excised tumors and healthy organs. Signals are normalized and displayed as rainbow plots overlaid on brightfield images. **f**, Relative quantification of fluorescent signal in liver, kidneys, and lungs normalized to tumor signal (Student's T-test analysis, two-tailed: *p = 0.017, **p(Liver: **DEATH-CAT-FNIR** v. **6QC-NIR)** = 0.003, **p(Liver: **DEATH-CAT-FNIR** v. **6QC-ICG**) = 0.006, **p(Lung: **DEATH-CAT-FNIR** v. **6QC-NIR**) < 0.001). Sample mean ± S.D., sample size (n) are as follows– **DEATH-CAT-FNIR**(liver): 0.7 ± 0.1, 4; **6QC-ICG**(liver): 1.1 ± 0.2, 4; **6QC-NIR**(liver): 3.0 ± 0.9, 4; **DEATH-CAT-FNIR**(kidneys): 1.0 ± 0.4, 4; **6QC-ICG**(kidneys): 1.1 ± 0.7, 4; **6QC-NIR**(kidneys): 2.7 ± 1.0, 4; **DEATH-CAT-FNIR**(lungs): 0.2 ± 0.1, 4; **6QC-ICG**(lungs): 0.2 ± 0.1, 4; **6QC-NIR**(lungs): 0.5 ± 0.0(4), 4. The data presented were acquired from four biological replicates.

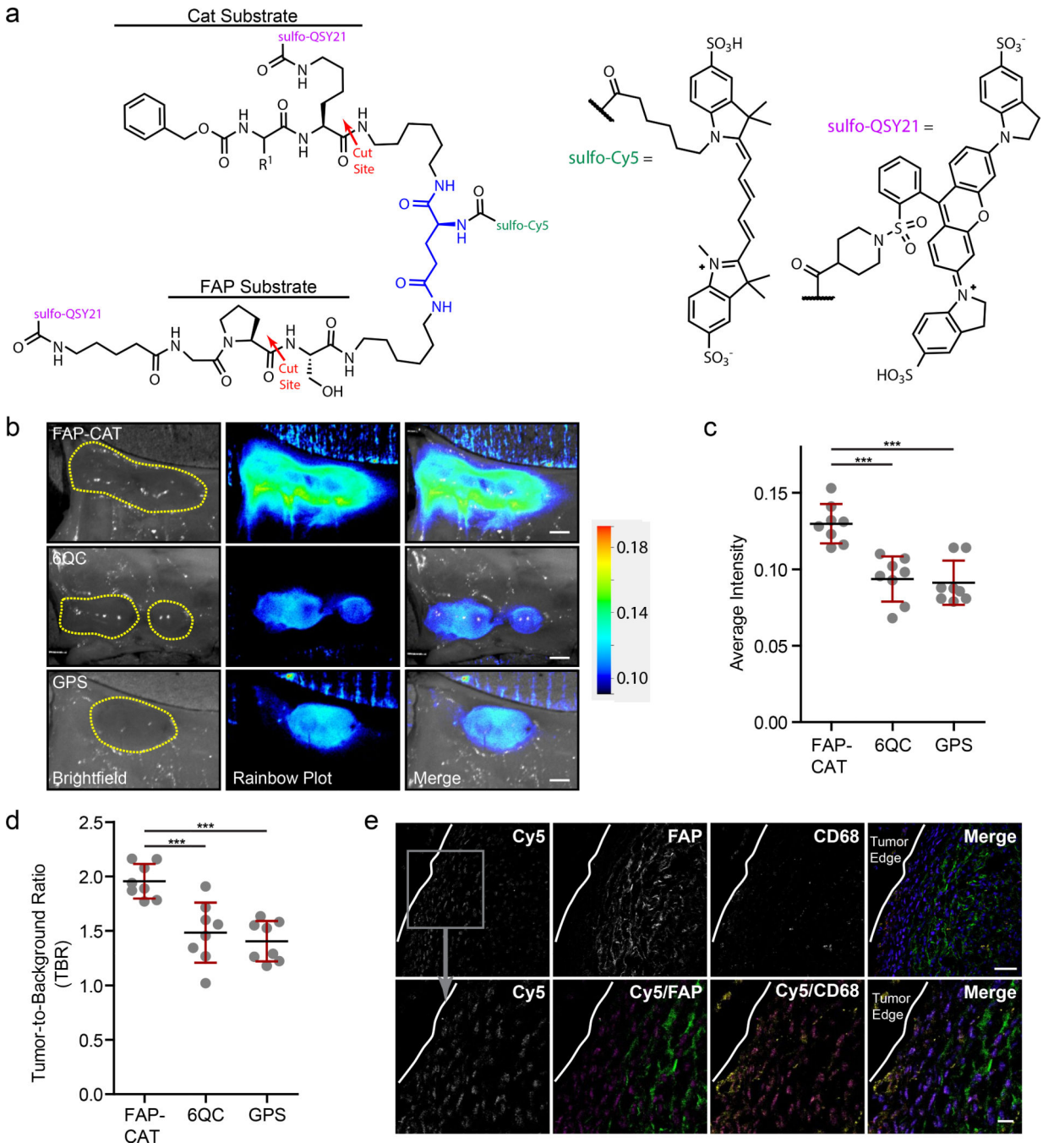

Fig. 6 |. Structure of the FAP-CAT AND-Gate probe and evaluation in a 4T1 breast tumor model. **a**, Structure of the **FAP-CAT** AND-Gate probe. **b**. Representative brightfield, rainbow plot, and overlay images of splayed 4T1 tumors 4 h post tail vein injection of **FAP-CAT**, **6QC**, and **GPS** (20 nmol). Yellow dotted lines outline the tumors in the brightfield images. **c**, Scatter plot of average fluorescence intensity of splayed tumors from each cohort (One-way ANOVA, Student's T-test analysis, two-tailed: ***p < 0.0001). Rainbow plots overlaid on brightfield images of all mice are representative of eight images from each cohort and can be found in the Supplementary Information. Sample mean ± S.D., sample size (n) are as

follows–**FAP-CAT**: 0.13 ± 0.01, 8; **6QC**: 0.9 ± 0.1, 8; **GPS**: 0.9 ± 0.1, 8. **d**, Scatter plot of TBR of splayed tumors from each mouse cohort receiving probe (One-way ANOVA, Student's T-test analysis, two-tailed: ***$p < 0.001$). Sample mean ± S.D., sample size (n) are as follows–**FAP-CAT**: 2.0 ± 0.2, 8; **6QC**: 1.5 ± 0.3, 8; **GPS**: 1.4 ± 0.2, 8. **e**, Immunofluorescence microscopy images of the edge of a 4T1 tumor dissected from a mouse injected with the **FAP-CAT** probe (top panel: scale bar = 50 μm, lower panel: scale bar = 10 μm). White line indicates the edge of the tumor. Single channel images are shown in gray scale. Merge images are as follows: Cy5 (probe) is magenta, CD68 is yellow, FAP is green, DAPI is blue. The same contrast and brightness settings were used to process each image. Images of additional examples of stained 4T1 tumor sections can be found in the Supplemental Information and are representative of 30 field of views. The data presented were acquired from four biological replicates.

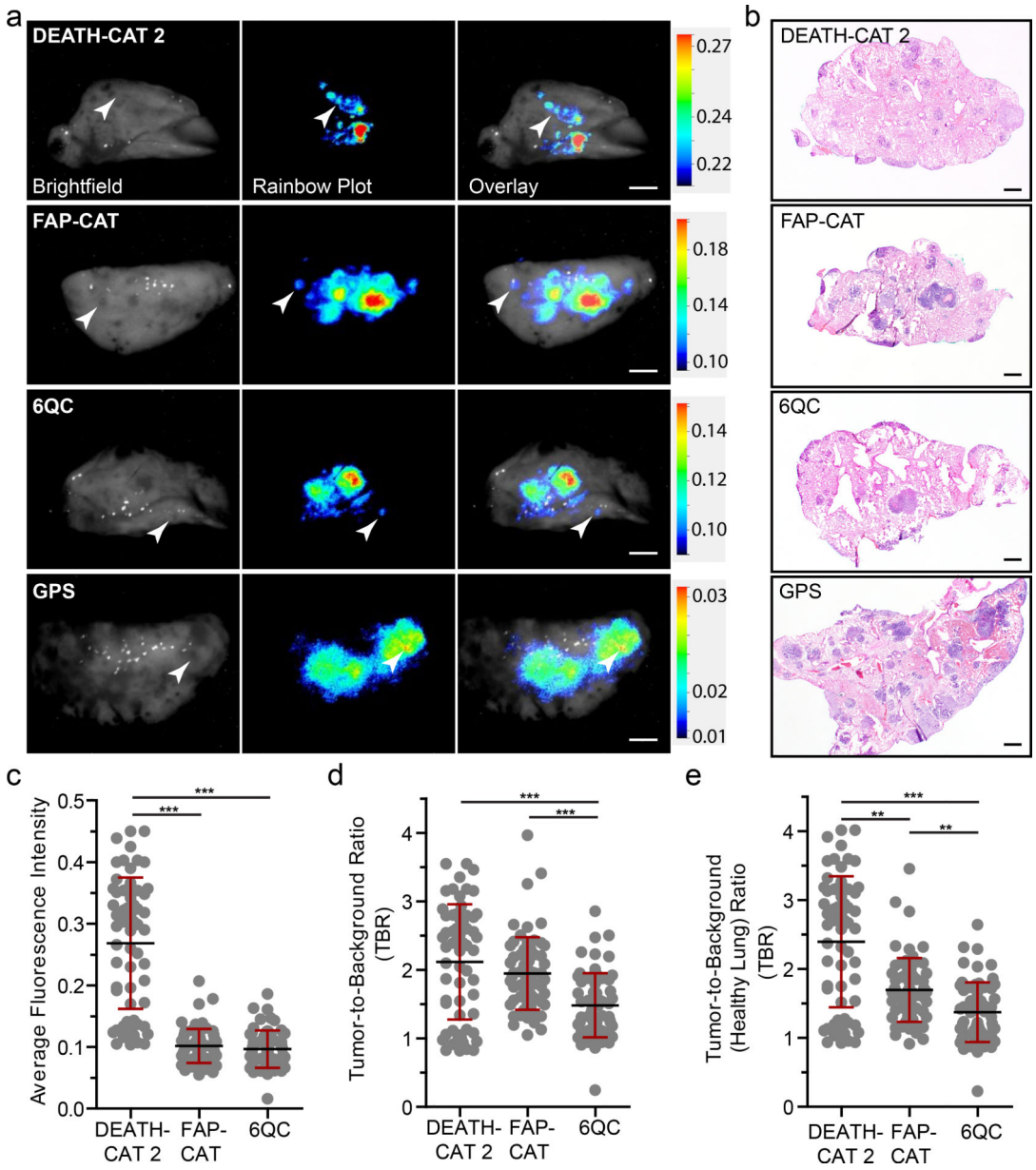

Fig. 7 |. Evaluation of AND-Gate probes in a mouse model of lung metastasis.

a, Representative brightfield, rainbow plot, and overlay images of resected lungs bearing metastases 16 h post tail vein injection of **DEATH-CAT 2**, **FAP-CAT**, **6QC**, and **GPS** (30 nmol). White arrows indicate example metastases. Scale bar = 3 mm. Four total images were taken for each cohort. **b**, Representative H&E staining of sections from imaged lungs bearing metastases. Scale bar = 1 mm. Images are representative of five sections stepwise through each tissue. **c**, Scatter plot of average fluorescent intensity within identified lung tumor nodules (Kruskal-Wallis,Dunn's multiple comparison test, multiplicity adjusted p-value: ***p < 0.0001). Sample mean ± S.D., sample size (n) are as follows–**DEATH-CAT 2**: 0.27 ± 0.11, 63; **FAP-CAT**: 0.10 ± 0.03, 66; **6QC**: 0.10 ± 0.03, 65. **d**, Scatter plot of TBR for tumors calculated using adjacent lung tissue (Kruskal-Wallis, Dunn's multiple comparison test, multiplicity adjusted p-value: ***p < 0.0001). Sample mean ± S.D., sample

size (n) are as follows–**DEATH-CAT 2**: 2.1 ± 0.8, 63; **FAP-CAT**: 2.0 ± 0.5, 66; **6QC**: 1.5 ± 0.5, 65. **e**, Scatter plot of TBR calculated using signals from healthy mouse lungs not bearing tumors (Kruskal-Wallis, Dunn's multiple comparison test, multiplicity adjusted p-values: **p(**DEATH-CAT 2** v. **FAP-CAT**) = 0.004, **p(**FAP-CAT** v. **6QC**) = 0.003, ***p < 0.0001). Sample mean ± S.D., sample size (n) are as follows–**DEATH-CAT 2**: 2.4 ± 1.0, 63; **FAP-CAT**: 1.7 ± 0.5, 66; **6QC**: 1.4 ± 0.4, 65. The data presented were acquired from three biological replicates.

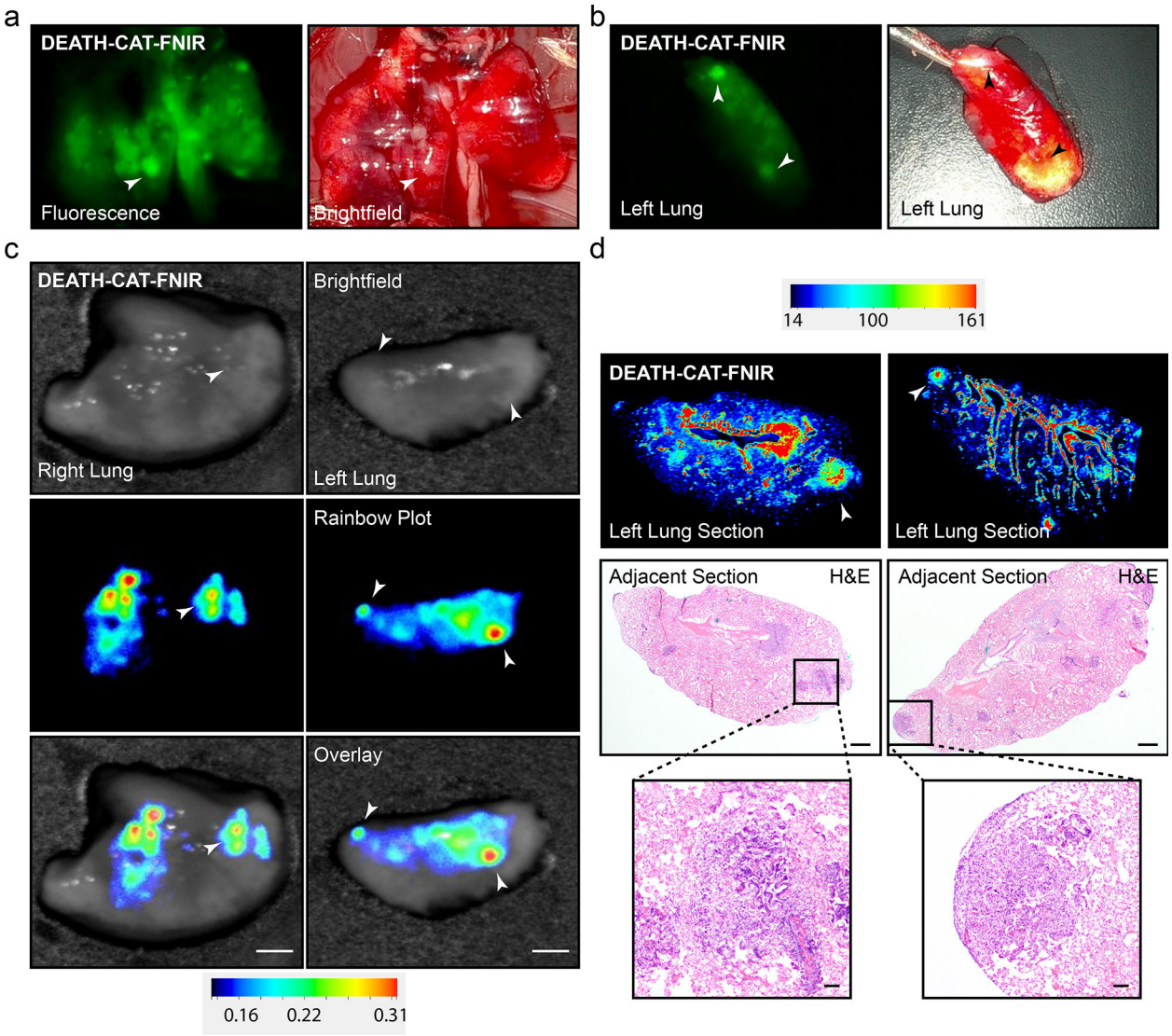

Fig. 8 |. Evaluation of DEATH-CAT-FNIR in a mouse model of lung metastasis.

a, Screen capture from recorded video on the da Vinci surgical robot with the FireFly detector. Images show screen capture of fluorescence (left) and brightfield (right) images of lungs bearing metastases 16 h post tail vein injection of **DEATH-CAT-FNIR** (20 nmol). **b**, Screen capture of *ex vivo* left lung bearing metastases 16 h post injection with **DEATH-CAT-FNIR** (20 nmol). White arrows indicate the same tumor nodules identified using all fluorescence detection modalities. **c**, Representative brightfield, rainbow plot, and overlay images of the resected lungs from (a) and (b). Scale bar = 3 mm. Images are representative of four total images. **d**, Rainbow plot images of unstained sections from the left lung from (**b**; top) and H&E stained adjacent sections (bottom, with inlays for tumor regions). Arrows indicate the location of the metastases identified in all imaging modalities. Scale bar = 1 mm. Zoom is 10X image of metastases identified in fluorescent scans. Scale bar = 100 μm. Images are representative of five sections stepwise through each tissue.